Available online at www.sciencedirect.com
ScienceDirect
Trans. Nonferrous Met. Soc. China 35(2025) 3617−3637
Transactions of Nonferrous Metals Society of China
www.tnmsc.cn

Prediction of temperature and strain rate dependent flow behaviors for AA6061-T4 sheet using phenomenology and machine learning-based approaches

Zhi-hao WANG[1], D. GUINES[1], Jia-shuo QI[2], Xing-rong CHU[3], L. LEOTOING[1]

1. Univ Rennes, INSA Rennes, LGCGM (Laboratoire de Génie Civil et Génie Mécanique) - EA 3913, F-35000 Rennes, France;
2. Alliance Sorbonne Université, Université de Technologie de Compiègne, Laboratoire Roberval, CS 60319, Compiègne Cedex, France;
3. School of Mechanical, Electrical and Information Engineering, Shandong University, Weihai 264209, China

Received 4 March 2024; accepted 26 August 2024

Abstract: The plastic flow behaviors of AA6061-T4 sheets at different temperatures (21−300 °C) and strain rates (0.002−4 s^{-1}) were studied. Significant nonlinear effects of temperature and strain rate on flow behaviors were revealed, as well as underlying micromechanical factors. Phenomenology and machine learning-based constitutive models were developed. Both models were formulated in the framework of a temperature-dependent linear combination regulated by a transition function to capture the evolution of strain-hardening behavior with increasing temperature. Novel mathematical functions for describing temperature and strain rate sensitivities were formulated for the phenomenological constitutive model. The threshold temperature related to microstructure evolution was considered in the modeling. A data-enrichment strategy based on extrapolating experimental data via classical strain hardening laws was adopted to improve neural network training. An efficient inverse identification strategy, focusing solely on the transition function, was proposed to enhance the prediction accuracy of post-necking deformation by both constitutive models.

Key words: AA6061-T4 sheet; thermo-visco-plasticity; constitutive model; machine learning; strain rate and temperature effects

1 Introduction

The increasing demand for lightweighting in industrial products has driven the integration of structural optimization and lightweight materials application. Aluminum alloys have emerged as a major lightweight material due to their unique combination of high specific strength and favorable thermo-formability [1]. In recent years, advanced hot forming techniques, such as heat treatment forming and in-die quench [2] and electrically-assisted manufacturing [3] have been developed to exploit the thermo-formability of aluminum alloys for the fabrication of complex components. During hot forming processes, aluminum alloys usually undergo complex microstructure evolution, which causes the influences of forming temperature and strain rate on their mechanical responses to be significant and nonlinear [4]. The choice of optimal process parameters for hot forming techniques requires a thorough understanding of the material's flow behavior at different temperatures and strain rates, as well as the aid of finite element analysis. Therefore, it is essential to formulate a suitable constitutive model for the selected aluminum alloy.

Corresponding author: L. LEOTOING, E-mail: lionel.leotoing@insa-rennes.fr
https://doi.org/10.1016/S1003-6326(25)66902-0

Over the years, numerous constitutive models are developed to represent the flow behaviors. In general, these models could be categorized into three types: physics, phenomenology, and machine learning (ML)-based models. The physical models are developed based on micro-mechanism of the crystal plastic deformation, and the internal variables of the model are directly associated with the dislocation dynamics, thermal activation, and microstructural evolution, such as ZERILLI−ARMSTRONG model [5] and VOYIADJIS−ABED model [6]. Developing a phenomenological constitutive model entails formulating appropriate mathematical functions to describe the observed material behaviors. These mathematical functions are usually simple in form, and yet provide a sufficient approximation to experimental observations. This makes the phenomenological models user-friendly. The recent trend has increased the focus on ML-based models [7]. The benefit of ML is that it eliminates the requirement to formulate a constitutive function, obviating the need for prior analysis of interrelations among strain hardening, temperature and strain rate.

A classical form of the phenomenological constitutive model is the Johnson−Cook framework, which is represented as a multiplicative combination of three terms including temperature, strain rate and strain as variables. In order to adapt the Johnson−Cook model more precisely for different alloys, numerous modifications have been proposed. WANG et al [8] modified the strain hardening term by considering the temperature and strain rate coupling factors to accommodate AA7075 at cryogenic temperatures. LIM−HUH model [9] introduced the effect of strain level in the strain rate term that can accurately describe the flow behaviors of 4043 steel and Ti6Al4V over a wide range of strain rates. PIAO et al [10] further improved the LIM−HUH model by incorporating a rate-dependent thermal softening term to represent the hardening behaviors at elevated temperatures. The quest for modifying and enhancing reflects the empirical nature of the phenomenological constitutive model, i.e., capturing the flow behaviors of specific alloys within a limited range of strain rates and temperatures. The mutual coupling among strain, temperature and strain rate variables is more often considered in the constitutive models developed in recent years. Considering the coupling effect of variables allows the constitutive model to predict the flow behavior of aluminum alloys more accurately. As reported by KHAN and BAIG [11], the strain rate sensitivity of AA5182-O exhibits a strong temperature dependence, with the strain rate sensitivity changing from negative at 20 °C to positive at 200 °C. The KHAN−LIU model [12] was developed for AA2024-T351 to capture the observed material behaviors: the strain hardening rate decreases with temperature, and the strain rate sensitivity becomes more pronounced when the temperature exceeds a threshold value. To improve the ability of models for predicting material necking and post-necking responses, SUNG et al [13] proposed the H/V model, that is based on a temperature-dependent linear combination of power law and saturation strain hardenings. The H/V model allows the transition from unbounded hardening at ambient temperature to saturation strain hardening behavior at elevated temperatures. Inspired by the H/V model, several studies [14,15] have used the similar linear combination framework to describe the flow behaviors of aluminum alloys.

In this work, the constitutive modeling of AA6061 at different temperatures and strain rates is pursued. AA6xxx is a series of precipitation hardened aluminum alloys [16]. The precipitates consist of silicon and magnesium solutes and are highly sensitive to temperatures. Studies have reported that effects of precipitates on the constitutive behavior of 6xxx aluminum alloys are significant, especially on the initial yield stress [17] and strain hardening behavior [18]. The modeling of the initial yield stress directly determines the accuracy of the constitutive model, as it defines the starting point of the hardening curve. In phenomenological constitutive models, the effects of temperature and strain rate on the initial yield stress are commonly assumed to be the same as those on strain hardening. However, this assumption is not applicable to AA6061 since non-monotonic temperature effects on the initial yield stress have been observed. Therefore, the need to formulate a yield stress function to capture this phenomenon is evident. Moreover, for AA6061, the strain hardening behavior at low and intermediate temperatures is associated with thermally activated

cross-slip [19], while at high temperatures, non-conservative dislocation motion becomes the dominant mechanism. Macroscopically, an increase in forming temperature results in a more pronounced saturation-type of strain hardening behavior. The underlying complex micro-mechanisms pose a challenge for the constitutive modeling of AA6061. Therefore, it is essential to formulate mathematical functions to capture the observed flow behaviors of AA6061 and take the temperature and strain rate sensitivities into account.

Uniaxial tensile (UT) test is the primary method for characterizing the flow behavior of sheet metals. Under the assumption of a homogeneous stress distribution, the direct calculation of flow stress from the experimentally measured tensile force is valid only before strain hardening degradation or necking occurs. For AA6061 sheets, the limited strain hardening observed at high temperatures results in necking at small strain levels, posing a challenge in determining the flow stress through the UT test. Currently, the widely adopted strategy to address this challenge is to utilize an inverse identification method [20] with finite element (FE) simulation. Inverse identification works by iteratively updating the constitutive parameters to achieve the best match between the FE predicted forces [21] or strain fields [14] and the experimental results. However, constitutive models often contain numerous parameters to enhance fitting capability and flexibility, leading to a huge time-cost for the inverse identification procedure. In this study, an alternative strategy is proposed, where inverse identification is conducted solely on a transition function containing three parameters. The transition function defines a linear combination of two constitutive equations with saturated and power-law strain hardening features, respectively. By optimizing the parameters of transition function, the hardening and necking behaviors of AA6061 sheets at different temperatures and strain rates can be accurately predicted.

As an extension of the inverse analysis strategy with the transition function, it is also introduced into the ML-based constitutive modeling. ANN is a nonlinear mapping algorithm of ML, which has shown great potential in constitutive modeling. It can learn the hidden patterns and trends within the training data, without using a priori knowledge or assumptions about the underlying mechanics of the material deformation [22,23]. The training of ANN requires a substantial amount of data, such as strain−stress pairs. Hot compression test is an effective approach of characterizing the constitutive behavior of materials at large strain levels and providing abundant stress−strain data for ANN training. Some works have demonstrated that neural networks trained based on hot compression test data exhibit higher accuracy compared to traditional constitutive models [24−26]. While for sheet metals, the flow stresses provided by UT tests is severely insufficient for the training of an ANN model. Therefore, LI et al [27] proposed an indirect data training approach for ANN-based constitutive modeling. The ANN model was coupled to finite element simulations to predict the forces of UT tests. Gradients are calculated based on the gap of the predicted and experimental forces for updating the network parameters. However, the huge training time-cost is a major obstacle, as each update of the network parameters requires performing full FE simulations. The solution proposed in this study is a linear combination of two ANN models using the transition function. The two ANN models provide saturation-type and power-law-type predictions of flow stresses, respectively. This solution achieves data enrichment by extrapolating the experimental hardening curves, and reduces the time-consumption of ML-based modeling while ensuring modeling accuracy.

The purpose of the current work is to perform constitutive modeling for AA6061-T4 sheets at different temperatures and strain rates using phenomenology and ML-based approaches. UT tests are carried out to explore the material flow behaviors over six temperatures ranging from 21 to 300 °C and three strain rates of 0.002, 0.2 and 4 s^{-1}.

2 Experimental

AA6061 sheets with a thickness of 2 mm were used in the current work. The sheets were treated to the T4 condition and then stored at ambient temperature for two years. Figure 1 shows the original microstructure of the AA6061-T4 sample, with an average grain size of 32 μm.

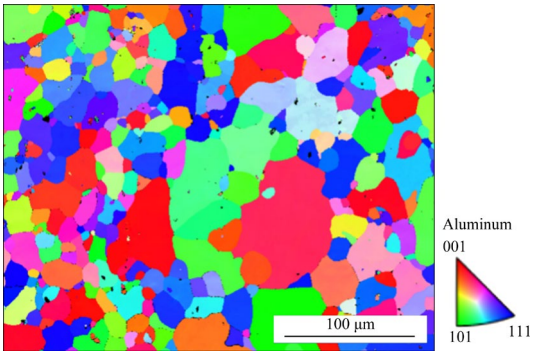

Fig. 1 Original microstructure of AA6061-T4 sheet by EBSD analysis

The effects of strain rate and temperature on the material constitutive behaviors were investigated by UT tests, which were conducted on a servo-hydraulic tensile machine equipped with a heating furnace, as shown in Fig. 2(a). Specimens were extracted from the sheet along the rolling direction by water jet cutting, and the specimen dimensions are shown in Fig. 2(b). The UT tests cover three strain rate levels: slow (0.002 s^{-1}), intermediate I (0.2 s^{-1}), and intermediate II (4 s^{-1}). To achieve the three strain rate levels, crosshead velocities were controlled to 0.1, 10, and 200 mm/s, respectively. For each strain rate, six testing temperatures are considered as 21, 119, 155, 190, 240 and 300 °C. The specimen was heated in the furnace from room temperature to the target temperature at rate of 30 °C/min, and held for 10 min before the test. The temperature at the center of the specimen was monitored by thermocouple wires. The grip device allows the release of the axial force due to thermal expansion of the specimen prior to stretching. The repeatability of the UT tests was verified. In order to apply the digital image correlation (DIC) method, a fast camera with a resolution of 128×688 pixels was used to record the deformation of the specimen with pre-painted patterns during the test. The acquisition frequency of the camera was adjusted according to the test duration so that 2000−3000 images were recorded during each test. The strain fields were calculated by the GOM software using a facet size of 14 pixels and a point distance of 7 pixels. For the electron backscatter diffraction (EBSD) measurements, the samples were prepared using the standard procedure of grinding and polishing. EBSD was operated at a voltage of 20 kV, working distance of 9 mm, a tilt angle of 70°, and a step size of 0.2 μm.

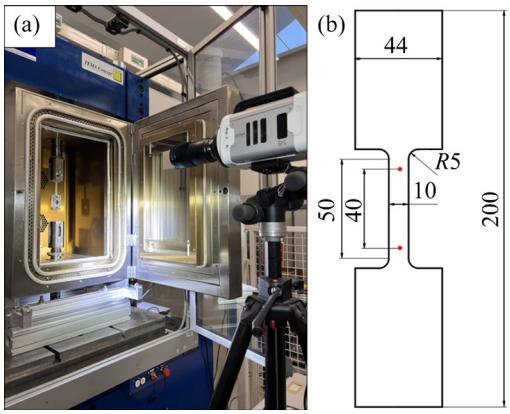

Fig. 2 (a) Servo-hydraulic tensile machine equipped with furnace and camera for application of DIC method; (b) Specimen dimensions (Red dots represent the location of the virtual extensometer; Unit: mm)

3 Results and discussion

3.1 Flow curves

The measured force−displacement (F−D) curves from the UT tests are shown in Fig. 3. The displacement refers to the elongation of the gauge section (length = 40 mm) as shown by red dots in Fig. 2 (b). All curves are plotted until the axial force suddenly drops. The true stress vs plastic strain curves up to the onset of necking are presented in Fig. 4. The true strain was calculated using a virtual extensometer created in the DIC post-processing with an initial gauge length of 40 mm. The initial yield stresses σ_0 (listed in Table 1) are determined with the 0.2% offset strain method.

As can be seen from Figs. 3 and 4, the temperature has a significant effect on the mechanical response of AA6061-T4 sheets in UT tests. Elevated temperatures enhance thermal activation, which reduces the required stress for the dislocation to overcome the energy barriers [28]. Macroscopically, the measured tensile strength exhibits a decrease with increasing temperature, and the strain hardening rate also decreases accordingly. At temperature of 300 °C, limited strain hardening occurs, and the measured axial force reaches a maximum almost immediately after the onset of deformation, followed by a subsequent softening. The strain hardening behaviors at low and intermediate temperatures are associated with thermally activated cross-slip [29], while at high

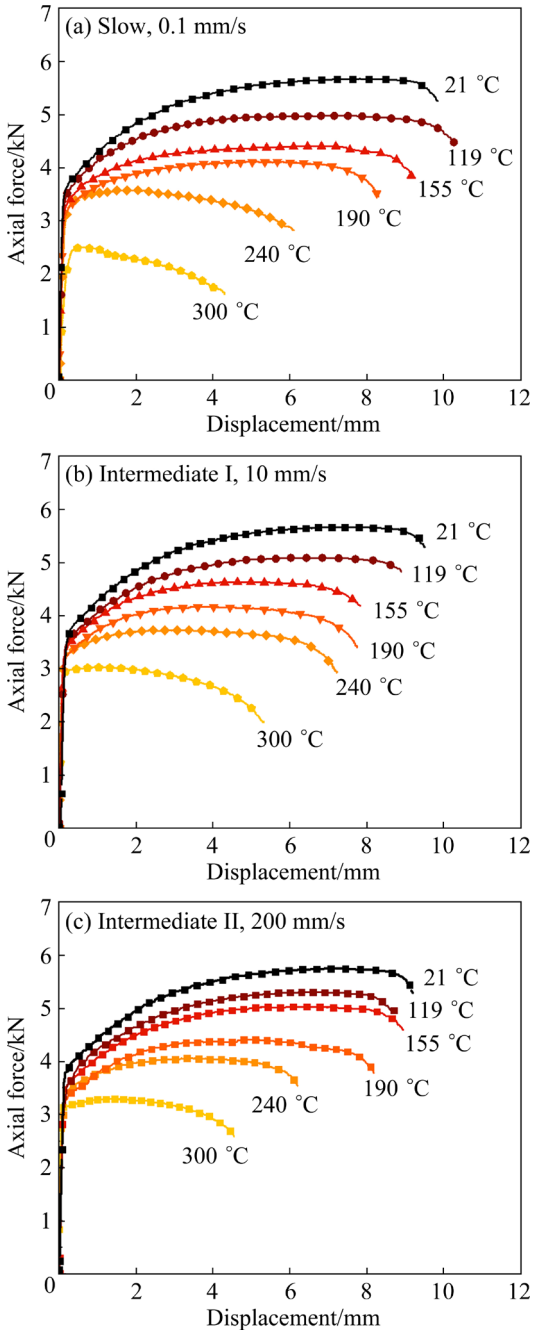

Fig. 3 F−D curves at different temperatures under slow (a), and intermediate I (b) and II (c) strain rate levels

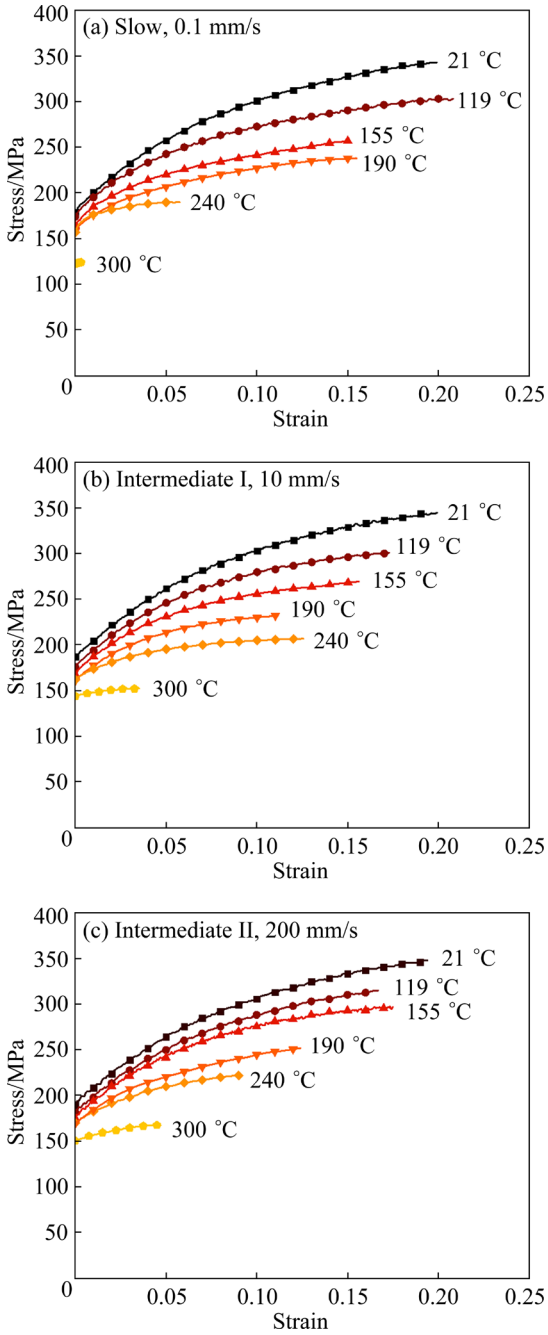

Fig. 4 True stress vs true plastic strain curves at different temperatures under slow (a), and intermediate I (b) and II (c) strain rate levels

temperatures, the vacancy-assisted dislocation climb becomes the dominant mechanism [19]. Figure 5 shows EBSD micrographs of the samples tested at 190 and 300 °C. The samples are extracted from the vicinity of the fracture of the deformed samples. The sample tested at 190 °C exhibits a geometrically ordered microstructure. Within some grains, internal orientation deviations are observed due to dislocation mobility, which indicates the formation and rotation of subgrains. At 300 °C, enhanced dislocation migration results in numerous subgrains with random orientations. These subgrains tend to increase in size at elevated temperatures, consequently leading to the saturation of strain hardening.

The precipitation strengthening with Mg- and Si-containing particles plays an important role in the mechanical properties of AA6061-T4 sheets,

Table 1 Initial yield stresses σ_0 of AA6061-T4 sheets

Temperature/°C	σ_0/MPa		
	0.002 s^{-1}	0.2 s^{-1}	4 s^{-1}
21	183.2	187.4	190.3
119	174.3	176.2	181.7
155	164.7	168.1	175.3
190	155.9	161.4	169.7
240	156.3	165.2	173.3
300	120.6	134.5	145.9

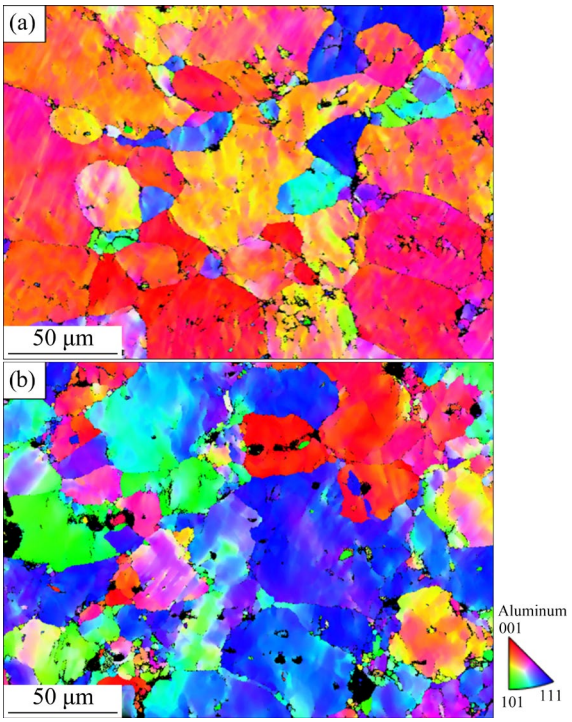

Fig. 5 IPF maps of AA6061-T4 samples tested at 190 °C (a) and 300 °C (b)

especially for the initial yield stress and work hardening [30]. The typical sequence of precipitation of the material is supersaturated solid solution → clusters → GP zones → β'' → β' → β (Mg_2Si) [31]. The β'' is commonly considered as the main strengthening phase [32], and its composition is found to be Mg_5Si_6 [33]. The distribution of β'' for the AA6061-T4 uniaxial stretched at 190 and 300 °C under slow strain rate level were investigated by the EBSD technique, as shown in Fig. 6. It can be found that the density of β'' (plotted in black) at 190 °C is higher than that at 300 °C. The β'' is almost fully dissolved at 300 °C, which could account for the significantly low initial yield stress and the weak strain hardening behavior. At room temperature and 119 °C, the flow stress exhibits a low strain rate sensitivity, while at elevated temperatures, the effect of strain rate becomes more pronounced. It is evident that AA6061-T4 has a temperature-dependent strain rate sensitivity. The decrease in initial yield stress shows non-monotonicity with increasing temperature. Specifically, the initial yield stress obtained at 240 °C is higher than that obtained at 190 °C, while the one obtained at 300 °C is lower. The non-monotonic variation in yield stress suggests the possibility of a complex underlying mechanism. The elevated yield stress at 240 °C could be attributed to the dynamic strain aging (DSA) effect, since a negative strain rate sensitivity is measured under low strain levels (<0.02). Similar results have been showcased for Al−Mg alloys in previous study [34].

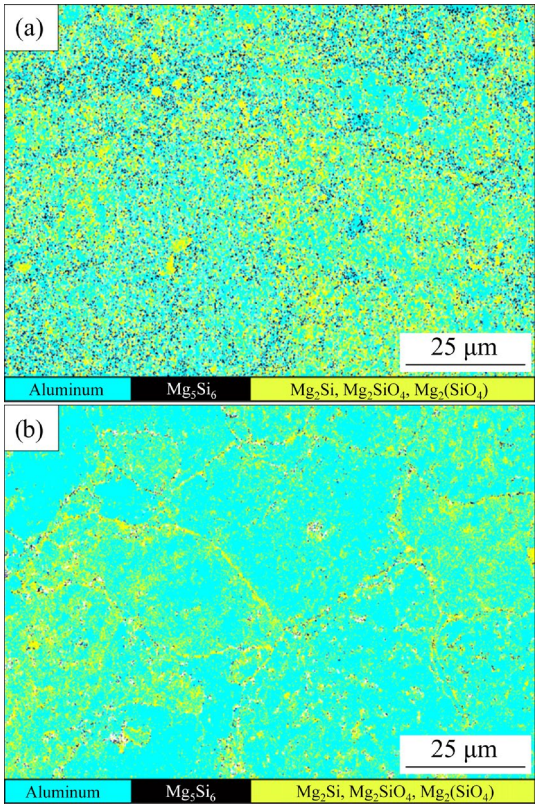

Fig. 6 Phase graphs of A6061-T4 samples tested at 190 °C (a) and 300 °C (b)

3.2 Phenomenological constitutive modeling

A new phenomenological constitutive model is proposed to represent the observed flow behaviors of AA6061-T4. In this model, the flow stress (Eq. (1)) is represented by the addition of an initial yield stress and a plastic strain-dependent stress

(referred to as hardening stress). With increasing temperature, the saturation characteristic of the strain hardening behavior of AA6061-T4 becomes more pronounced. To capture this transition of the strain hardening behavior, a temperature-dependent linear combination of saturation and power law strain hardening models is adopted. A transition function (Eq. (2)) is proposed to define the temperature-dependent coefficient (α) of the linear combination, which determines the change of strain hardening behavior between the power law (α=0) and saturation (α=1) with respect to temperature.

$$\sigma=\sigma_0(T,\dot{\varepsilon})+\alpha(T)\cdot\sigma_{sat}+[1-\alpha(T)]\cdot\sigma_{pow} \quad (1)$$

$$\alpha(T)=P_1+(1-P_1)\cdot\tanh\left[(T-T^*)^{P_2}/(T_m-T)\right]^{P_3} \quad (2)$$

where T^* and T_m are the reference and melting temperatures, respectively. In this work, the reference temperature is selected as 21 °C, and the melting temperature adopts 652 °C. The coefficient $\alpha\in[0, 1]$, P_1, P_2 and P_3 are model parameters, σ_{sat} is the hardening stress predicted by the saturation model, and σ_{pow} is the hardening stress predicted by the power law model.

3.2.1 Initial yield stress

The initial yield strength is an important property indicator of materials since it is considered as the material's failure point in many engineering scenarios. For the investigated material, the initial yield stress is mainly influenced by thermal softening and strain rate hardening. In addition, a non-monotonic relationship with the increasing temperature is observed at about 240 °C, which could be attributed to the DSA effect. Therefore, the proposed initial yield stress function is formulated by additively decomposing these factors into a thermal softening component (f_{TS}) and a DSA component (f_{DSA}), as defined by Eq. (3) and illustrated in Fig. 7(a). The thermal softening component (Eq. (4)) is derived from the RUSINEK−KLEPACZKO model [35], which was originally developed to describe the variation of Young's modulus with temperature. A strain rate correction term is added to the thermal softening component to account for the strain rate hardening. The DSA component (Eq. (5)) was proposed by SHEN et al [36], which defines the contribution of DSA effect on the initial yield stress as a bell-shaped distribution with temperature.

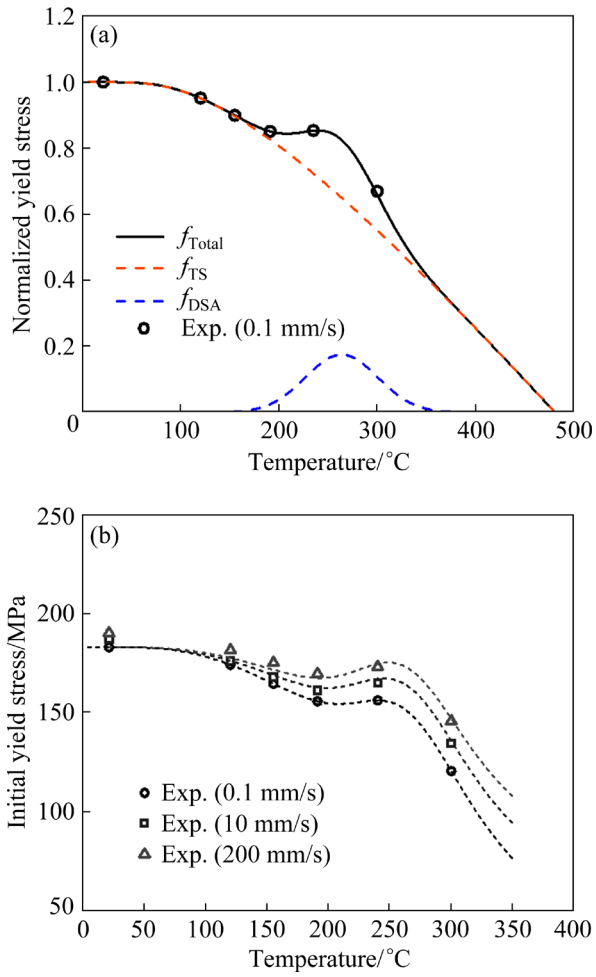

Fig. 7 (a) Curves of f_{Total}, f_{TS} and f_{DSA} calculated according to Eqs. (3)−(5), respectively; (b) Predictions of initial yield stress function in comparison with experimental results

$$\sigma_0(T,\dot{\varepsilon})=\sigma_0^*\cdot f_{Total}=\sigma_0^*\cdot(f_{TS}+f_{DSA}) \quad (3)$$

$$f_{TS}=\left\{1-\frac{T}{C_2}\cdot\exp\left[C_1\cdot\left(1-\frac{C_2}{T}\right)\right]\right\}^{1-C_3\cdot\ln\frac{\dot{\varepsilon}}{\dot{\varepsilon}^*}} \quad (4)$$

$$f_{DSA}=C_4\cdot\exp\left[-\left(\frac{T-C_5}{C_6}\right)^2\right] \quad (5)$$

where $\dot{\varepsilon}$ is the current strain rate, and the reference $\dot{\varepsilon}^*$ takes 0.002 s^{-1}. The initial yield stress determined under T^* and $\dot{\varepsilon}^*$ is selected as the reference yield stress σ_0^* (183.2 MPa). C_1−C_6 are material parameters. C_1, C_2 and C_3 in f_{TS} relate to the effects of temperature and strain rate on initial yield stress. C_4 defines the peak intensity of DSA effect, and C_5 defines the characteristic temperature corresponding to the peak intensity of DSA. C_6

relates to the variation of DSA effect with temperature. The fitting results of the proposed model to the experimental initial yield stresses are shown as dashed lines in Fig. 7(b), and the identified parameters are listed in Table 2.

Table 2 Calibrated parameters of initial yield stress function for AA6061-T4 sheets

C_1	C_2/°C	C_3	C_4	C_5/°C	C_6/°C
0.544	481	0.0514	0.175	263.7	52

3.2.2 Saturation model

When α=1, the constitutive model reduces to Eq. (6). The saturation model (σ_{sat}) takes an exponential form, expressed in Eq. (7), which allows the hardening stress to saturate at large strain levels. The increment of flow stress from the initial yield stress to the saturation stress is referred to here as the plastic saturation stress (σ_s):

$$\sigma=\sigma_0(T)+\sigma_{sat} \tag{6}$$

$$\sigma_{sat}=A_v\cdot\left[1-\exp\left(-B_v\cdot\varepsilon_p\right)\right]^{C_v} \tag{7}$$

where ε_p is the equivalent plastic strain, A_v directly determines the plastic saturation stress, and C_v relates to the rate at which the hardening stress tends to saturation. The larger C_v leads to a smaller hardening rate in the initial stage. An example is provided in Fig. 8 to show the effect of C_v, where C_v_1 is larger than C_v_2. B_v is a material constant independent of temperature and strain rate, which can be obtained by fitting Eq. (6) to true stress vs plastic strain at the reference temperature and strain rate.

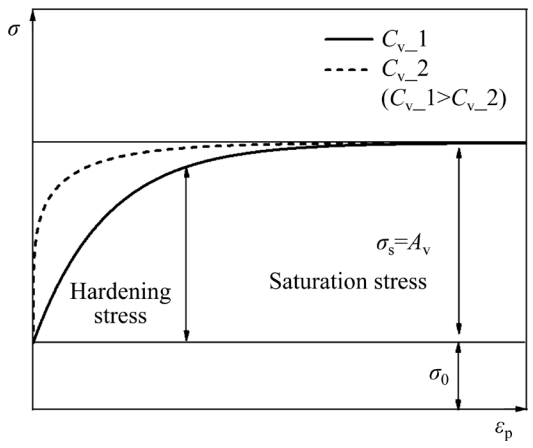

Fig. 8 Schematic representation showing effect of A_v and C_v on stress−plastic strain curves

The effect of T and $\dot{\varepsilon}$ on the plastic saturation stress (σ_s) is expressed in function A_v through a multiplicative framework, as given in Eq. (8). In this work, σ_s of each test condition is determined by fitting Eq. (6) to the corresponding true stress vs plastic strain.

$$A_v=\sigma_s^*\cdot f_v(T)\cdot g_v(\dot{\varepsilon},\ T) \tag{8}$$

where σ_s^* is the plastic saturation stress at T^* and $\dot{\varepsilon}^*$, $f_v(T)$ defines the temperature softening, and $g_v(\dot{\varepsilon},T)$ defines the strain rate hardening. $g_v(\dot{\varepsilon},T)$ reduces to unity at $\dot{\varepsilon}^*$.

To quantitatively analyze the thermal softening effect on plastic saturation stress, the experimental values of σ_s/σ_s^* at different temperatures under the reference strain rate are calculated, as plotted in Fig. 9. A relatively uniform decrease for σ_s is observed from 21 to 190 °C, while a pronounced decrease occurs above 190 °C. This discrepancy could be attributed to the evolution of microstructure during the deformation at elevated temperatures, including the shift of dislocation kinematic mechanisms and the dissolution of β'' precipitation. This behavior is seldom captured by existing phenomenological models, and is the motivation for the current model development. In this work, a critical temperature (T_c) is assumed, which can be interpreted as the temperature at which the microstructure evolution causes significant changes in stress responses. The temperature ranges below and above the critical temperature are described separately with f_{lt} and f_{ht} functions, and the entire temperature range is modeled by a harmonic average form:

$$\frac{1}{f_v(T)}=\frac{1}{f_{lt}(T)}+\frac{1}{f_{ht}(T)} \tag{9}$$

$$f_{lt}(T)=1-\tanh\left[\left(T-T^*\right)\Big/\left(T_m-T\right)^{k_0}\right] \tag{10}$$

$$f_{ht}(T)=\exp[-k_1\cdot(T-T_c)] \tag{11}$$

where k_0 and k_1 are model parameters. The curves of f_v, f_{lt} and f_{ht} are plotted in Fig. 9, and the critical temperature (T_c) for AA6061-T4 is identified as 218.5 °C. It can be seen that f_{lt} shows a relatively smooth decrease, while f_{ht} provides a rapid decrease above the critical temperature. In addition, both curves remain positive and tend to zero at the melting temperature. For the transition region around T_c, the harmonic average between the f_{lt} and f_{ht} agrees well with the experimental result.

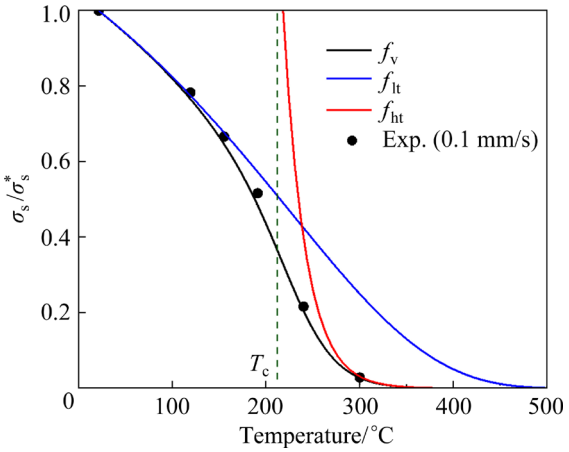

Fig. 9 Curves of f_v, f_{lt} and f_{ht} calculated according to Eqs. (9)−(11), respectively, and comparison with experimental results at different temperatures and slow strain rates

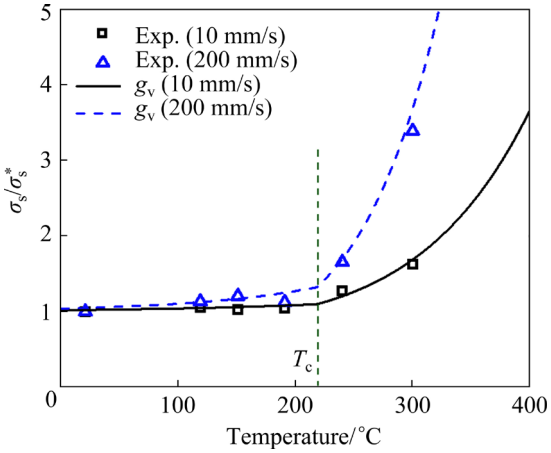

Fig. 10 Calculated values of σ_s/σ_s^* according to Eq. (12) in comparison with experimental results at different temperatures and intermediate I and II strain rates

Afterwards, the values of σ_s/σ_s^* at different temperatures under the intermediate I and II strain rate levels are calculated. The ratios of σ_s/σ_s^* at the intermediate I and II strain rates to the one at the reference strain rate are plotted in Fig. 10. The ratio ρ corresponds to the proportional change in σ_s due to temperature-dependent strain rate hardening effect as defined by g_v in Eq. (8). As can be seen from Fig. 10, there is also a critical temperature that distinguishes the strength of the strain rate hardening effect, and the effect is more significant at temperatures above the critical temperature. It is interesting to note that this critical temperature is similar to the one obtained from the fitting result of Eq. (11). Therefore, the formulation of g_v follows a function of both strain rate and temperature and takes into account the critical temperature T_c, as given in Eq. (12):

$$g_v(\dot{\varepsilon},\ T)=1+m_0\cdot\ln\left(\frac{\dot{\varepsilon}}{\dot{\varepsilon}^*}\right)^{m_1+m_2T}\cdot\left[1+m_3\cdot\frac{(T-T_c)+|T-T_c|}{T_m-T^*}\right] \tag{12}$$

where m_0, m_1, m_2 and m_3 are model parameters, and m_3 defines the proportional amplification of the strain rate hardening effect at temperatures above T_c.

In Eq. (7), C_v relates to the strain hardening behavior. The value of C_v for each test condition is determined by fitting Eq. (6) to the corresponding true stress vs plastic strain. Figure 11(a) illustrates the effect of T and $\dot{\varepsilon}$ on strain hardening behavior,

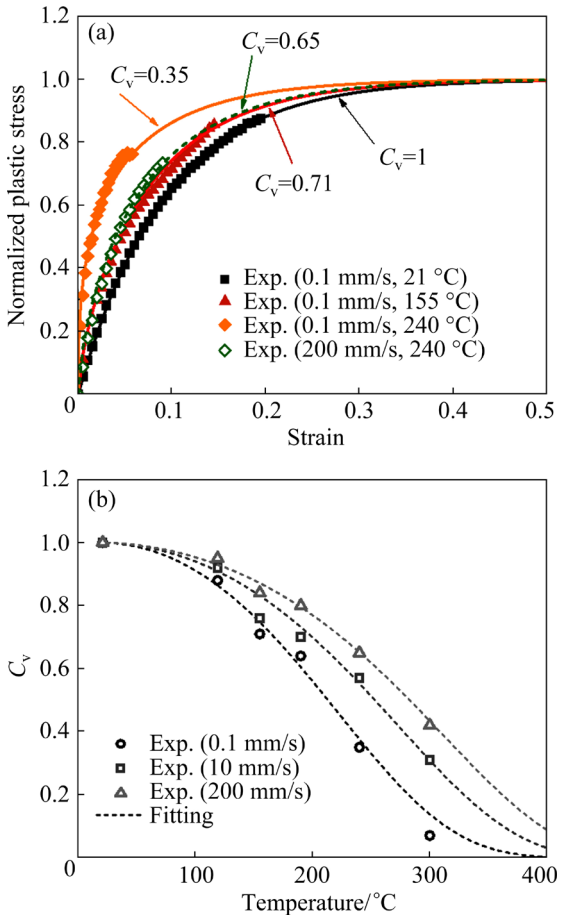

Fig. 11 (a) Effect of T and $\dot{\varepsilon}$ on strain hardening behavior, and corresponding change in C_v; (b) Values of C_v predicted by Eq. (13) compared with experimental results at different temperatures and strain rates

as well as the corresponding change in C_v. For visibility, only the results for 21, 155 and 240 °C at the slow strain rate and 240 °C at the intermediate

II strain rate are plotted. It can be seen that the increase in temperature causes the normalized hardening stress to saturate at a large initial rate, while the increase in strain rate brings the opposite effect. For C_v, its value decreases with increasing temperature and increases with increasing strain rate. The fitted C_v curves for different test conditions are plotted as symbols in Fig. 11(b). In order to describe the dependency of C_v on temperature and strain rate, a function of C_v (T, $\dot{\varepsilon}$), is proposed, and can be expressed as follows:

$$C_v(T,\ \dot{\varepsilon}) = \exp\left[-\left(\frac{(T-T^*)^{k_2-m_4\cdot\ln(\dot{\varepsilon}/\dot{\varepsilon}^*)}}{T_m-T}\right)^{k_3}\right] \quad (13)$$

where k_2, k_3 and m_4 are model parameters. The function allows the value of C_v to range from 1 to 0 from the reference temperature T^* to the melting temperature T_m.

The parameters involved in the developed saturation model can be classified as temperature-dependent parameters k_i and T_c, and strain rate-dependent parameters m_i. A combined optimization algorithm of particle swarm optimization (PSO) and SIMPLEX is used for parameters identification. The identification procedure is implemented on the mode-FRONTIER platform, and the gap between the model predicted and the experimental flow stresses is calculated by a MATLAB code. The following parameter identification strategy is adopted.

Step 1: With C_v as 1, the parameters B_v and σ_s^* are identified by fitting Eq. (6) to the true stress vs plastic strain data at the reference temperature (21 °C) and strain rate (0.002 s^{-1}).

Step 2: The parameters k_1, k_2, k_3, k_4 and T_c are identified using the true stress vs plastic strain data at different temperatures and reference strain rates.

Step 3: The parameters m_0, m_1, m_2, m_3 and m_4 are identified using the true stress vs plastic strain data at different temperatures and strain rates.

The identified parameters are listed in Table 3, and the total time-cost for parameter identification was about 50 min. The predicted flow stress curves of the proposed saturation model under different test conditions are plotted as colored lines in Fig. 12, and the experimental results are plotted as symbols for comparison. It is shown that the model represents well the flow stress with variation of temperatures and strain rates.

Table 3 Calibrated parameters of saturation model for AA6061-T4 sheets

σ_s^*/MPa	k_0	k_1/°C^{-1}	k_2	k_3	T_c/°C
185.4	0.9652	0.04209	1.115	1.652	218.5
m_0	m_1	m_2/°C^{-1}	m_3	m_4	B_v
0.002853	1.326	0.004625	10.98	0.01223	10.66

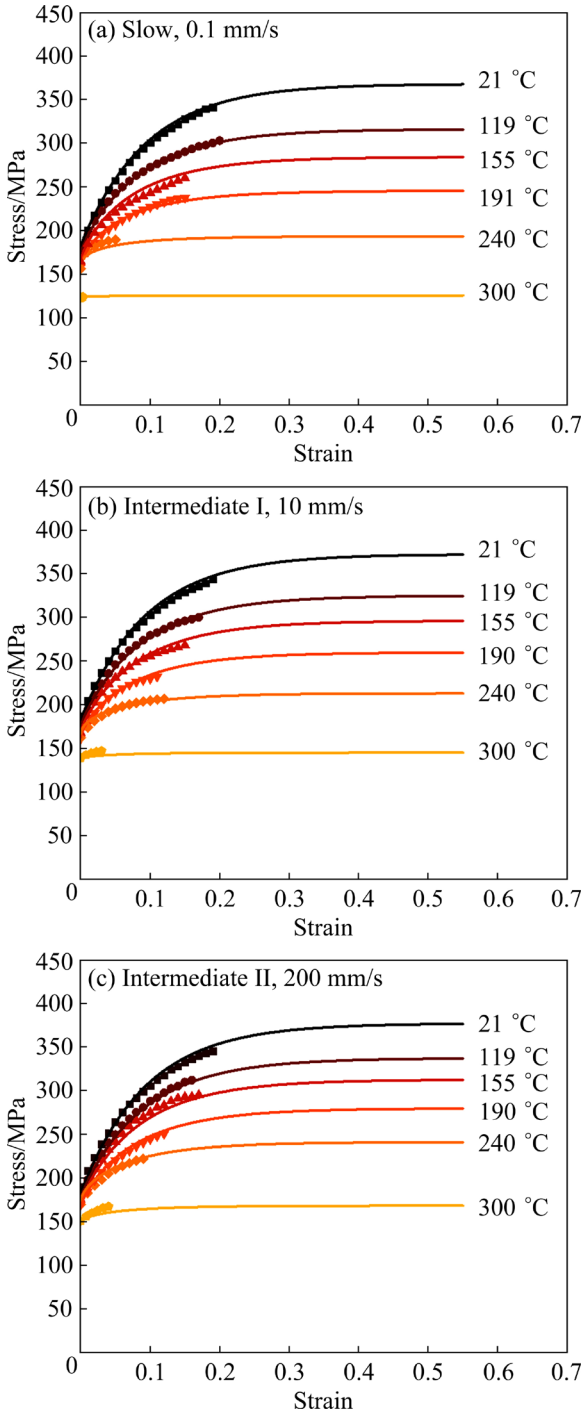

Fig. 12 Predicted flow stress curves (colored lines) by saturation model and experimental results (symbols) at different temperatures under slow (a), and intermediate I (b) and II (c) strain rates

3.2.3 Power law model

When α=0, the constitutive model reduces to Eq. (14). The power law model (σ_{pow}) is expressed by Eq. (15). The component R considers the thermal softening and strain rate hardening by means of a multiplicative framework, as given in Eq. (16). A power law form of $\dot{\varepsilon}/\dot{\varepsilon}^*$ is adopted to describe the strain rate hardening effect, which has been employed in some classical constitutive models, such as LIN−WAGONER [37], MOLINARI−RAVICHANDRAN [38], and KHAN−HUANG−LIANG [39] models. The thermal softening is described by means of the proposed function (Eq. (10)).

$$\sigma=\sigma_0(T)+\sigma_{pow} \tag{14}$$

$$\sigma_{pow}=R\cdot\varepsilon_p^n \tag{15}$$

$$R=v_0\left\{1-\tanh[(T-T^*)/(T_m-T)^{v_1}]\right\}\cdot\left(\frac{\dot{\varepsilon}}{\dot{\varepsilon}^*}\right)^{v_2+v_3\cdot T} \tag{16}$$

where v_0, v_1, v_2, v_3 and n are model parameters. The predicted flow stresses based on the power law model at different temperatures and strain rates are presented in Fig. 13, and the experimental results are plotted as symbols. The values of model parameters are listed in Table 4, which are identified simultaneously by the SIMPLEX algorithm on the mode-FRONTIER platform.

Table 4 Calibrated parameters of power law model for AA6061-T4 sheets

v_0/MPa	v_1	v_2	v_3/°C^{-1}	n
358.5	0.9712	0.01394	0.0000605	0.5

3.2.4 Calibration of transition function

Having defined σ_{sat} and σ_{pow} in Eq. (1), the parameters of the transition function (Eq. (2)) are then calibrated through a hybrid experimental-numerical inverse analysis [40]. The transition function regulates the strain hardening behavior at large strain levels presenting as saturation or power law or intermediate cases. In UT tests, the strain hardening is the primary material factor resisting necking [41], and necking leads to the decreasing stage of the F−D curve. Therefore, in this work, the parameters of the transition function are identified by minimizing gaps between the experimental and predicted F−D curves of UT tests.

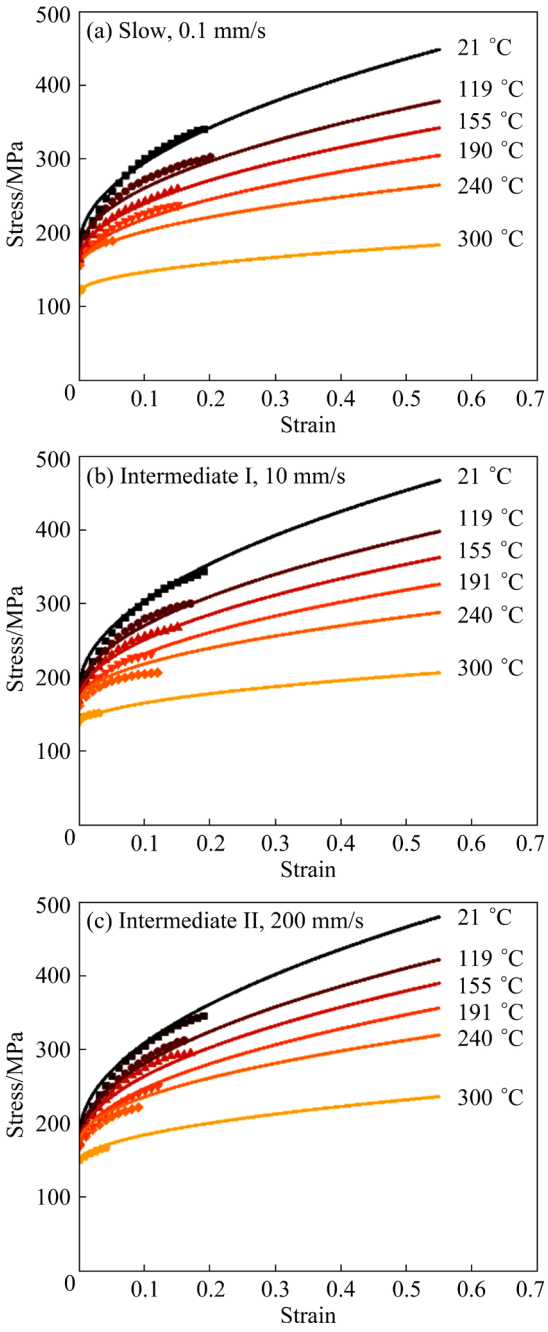

Fig. 13 Predicted flow stress curves (colored lines) by power law model and experimental results (symbols) at different temperatures under slow (a), and intermediate I (b) and II (c) strain rates

The numerical UT tests are conducted using ABAQUS/standard 2D code, as shown in Fig. 14. To trigger necking, a geometric imperfection is introduced in specimen modeling [42]. The width of the specimen central section is reduced by 0.002 mm, while the thickness remains constant. The finite element model of specimen is discretized through S4R elements with hourglass control, and

the mesh size in the specimen gauge section is refined to 0.5 mm. The specimen is loaded by applying experimental velocities, and the initial temperature of specimen is predefined according to the measured temperature at the beginning of tension. For the numerical UT tests at intermediate I and II strain rate levels, the coupled thermo-mechanical simulations are adopted to consider the plastic heat, and the specimen surfaces are treated as adiabatic condition. For the slow strain rate level, the specimen is treated as isothermal condition. The adiabatic temperature rise due to plastic work is calculated by

$$\Delta T=\frac{\eta}{\rho\cdot C_P}\int\sigma\cdot\mathrm{d}\varepsilon_{\mathrm{p}} \tag{17}$$

where η is a fraction of heat conversion caused by plastic deformation, ρ is the mass density, and C_p is the specific heat capacity. In this work, the value of η is assumed as 0.9 [13]. C_p adopts a linear variation from 0.897 J/(g·K) at 21 °C to 1.12 J/(g·K) at 300 °C [43].

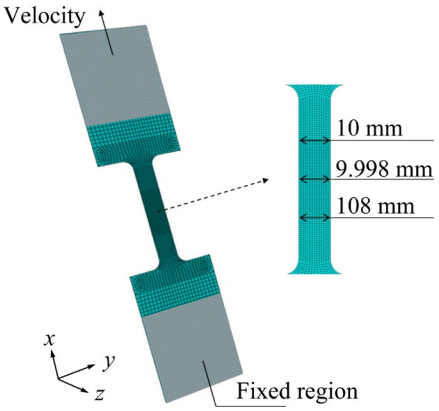

Fig. 14 Finite element model for UT test discretized with S4R elements, and introduced geometric imperfection

The proposed constitutive model is implemented in finite element simulations using the user subroutine UMAT, and the associated flow-rule based on Yld2000-2D anisotropy yield criterion [44] is employed. The Yld2000-2D parameters of α_1−α_8 listed in Table 5 for the investigated material are calibrated using the normalized yield stresses at a plastic work of 15 MJ/m^3 and average r-values determined by UT tests along 0°, 45° and 90° to the rolling direction as well as a bulge test at ambient temperature and strain rate of 0.002 s^{-1}. In Fig. 15, the predicted normalized yield stresses and r-values by Yld2000-2D are plotted alongside the experimental results. It should be noted that the effects of temperature and strain rate on material anisotropy are neglected in this work.

Table 5 Yld2000-2D parameters for AA6061-T4 calibrated at ambient temperature

α_1	α_2	α_3	α_4	α_5	α_6	α_7	α_8
0.947	0.922	0.941	0.998	1.007	0.902	0.964	1.076

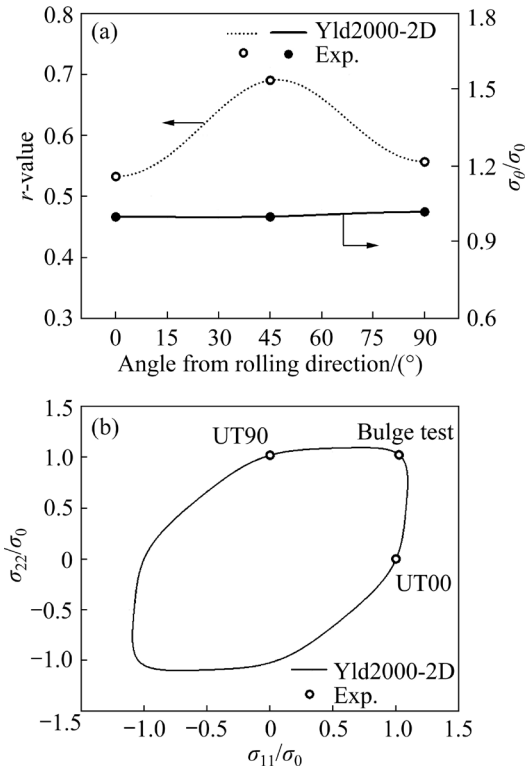

Fig. 15 (a) Experimental and Yld2000-2D predicted normalized yield stresses and r-values; (b) Normalized plane stress yield locus

During the hybrid experimental−numerical inverse analysis, the parameters P_i of the transition function are iteratively updated to minimize the gap between the experimental and predicted F−D curves. The displacement refers to the elongation of the specimen gauge section. The gap is quantified by a cost-function:

$$Q(P_i)=\frac{1}{N_{\mathrm{T}}+N_{\mathrm{R}}}\sum_{t,r=1}^{N_{\mathrm{T}},N_{\mathrm{R}}}\left(\frac{1}{N_{\mathrm{I}}}\sum_{i=1}^{N_I}\frac{\left|F_i^{\mathrm{num}}-F_i^{\mathrm{exp}}\right|}{F_i^{\mathrm{exp}}}\right) \tag{18}$$

where N_{T}=6 and N_{R}=3 are the numbers of temperature and strain rate conditions, respectively. N_{I} is the total number of equally spaced displacement points (at least 50 points) defined in each experimental curve.

The calibrated parameters P_i are listed in Table 6, and the final value of cost-function is close to 3%. The time-cost for the inverse identification procedure was about 70 h. The computation time with the phenomenological model is about 3 min per FE job. The curve of the transition function which presents the evolution of coefficient α with temperature is shown in Fig. 16. The parameter P_1 determines the hardening behavior for low temperature ranges. P_2 and P_3 control the temperature at which the hardening behavior transitions and the corresponding rate of this transition. The flow stresses under different test conditions predicted by the calibrated phenomenological constitutive model are shown as colored lines in Fig. 17. By referring to the experimental results, it is shown that the proposed constitutive model well captures the stress responses of AA6061-T4, including initial yield stress and flow stress. The strain levels for the localized necking stage of uniaxial tensile tests under different test conditions are shown as short dashed lines in Fig. 17. The inverse analysis procedure calibrates the constitutive model up to these strain levels, while the predicted flow stresses beyond these strain levels are the extrapolation parts. For the extrapolation parts, the constitutive model provides the following predictions: below 155 °C, the strain hardening behavior is an intermediate state between the power law and saturation; from 155 to 300 °C, the strain hardening behavior transitions from the intermediate state to saturation. Figure 18 presents the predicted (colored lines) and experimental (symbols) F−D curves. For the slow and intermediate I strain rates, the predicted curves agree well with the experiments, and the necking phenomena at different temperatures are well captured. The gradual decrease of the axial force at 240 and 300 °C after

Table 6 Calibrated parameters of transition function for phenomenological constitutive model

P_1	P_2	P_3
0.65	1.32	22.3

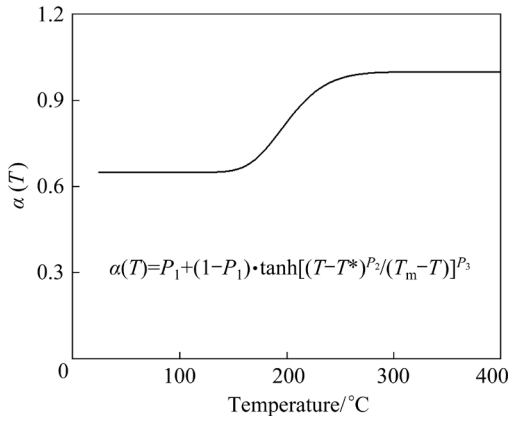

Fig. 16 Evolution of linear combination coefficient α with temperature calculated with parameters listed in Table 6

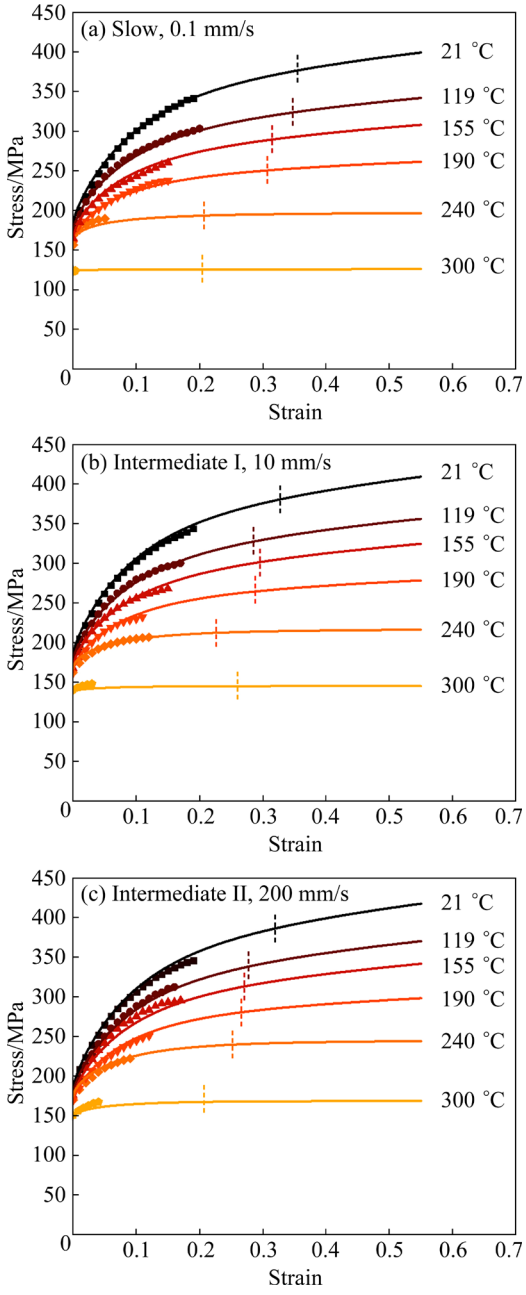

Fig. 17 Predicted flow stress curves (colored lines) by phenomenological constitutive model and experimental results (symbols) at different temperatures under slow (a), and intermediate I (b) and II (c) strain rate levels

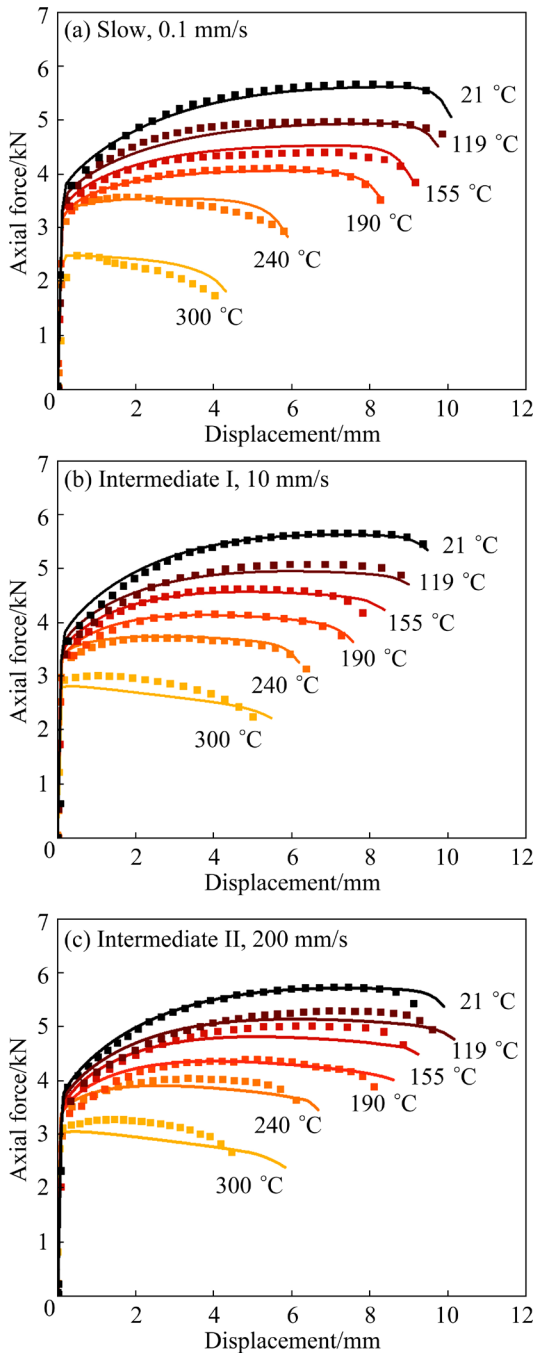

Fig. 18 Predicted (colored lines) and experimental (symbols) F−D curves for UT tests at slow (a), and intermediate I (b) and II (c) strain rate levels (The predictions are obtained from the phenomenological constitutive model)

reaching the force maximum is correctly reproduced. For the intermediate II strain rate level, the calibrated constitutive model provides qualitatively reasonable predictions of the material behavior. From 21 to 240 °C, the necking is correctly predicted. While, the prediction for the 300 °C case underestimates the axial force by about 0.31 kN, and the predicted localized necking is delayed. Overall, the proposed constitutive model effectively represents the flow stresses of AA6061-T4 at different temperatures and strain rates, and the defined transition in strain hardening behavior with temperature provides a reasonable prediction of necking.

3.3 Machine learning-based modeling

The effects of temperature and strain rate on the constitutive behaviors for AA6061-T4 are highly nonlinear, which results in the development of the phenomenological constitutive model being complex and time-consuming, as seen in the previous section. ANN offers an alternative approach to constitutive modeling, obviating the need for prior analysis of interrelations among strain hardening, temperature, and strain rate. However, the ANN model requires sufficient experimental data for training to achieve optimal performance. As illustrated in Fig. 4, the experimental determined flow stresses at elevated temperatures are limited to quite low strain levels, potentially causing distorted predictions by the ANN model. An optimal solution is to extrapolate the experimental data at different temperatures and strain rates using the classical phenomenological hardening laws. In this work, the Voce and Ludwick hardening laws are used to generate two datasets. These two datasets are then employed for training two ANN models. Therefore, the two ANN models exhibit saturation and power law behavior for the prediction of flow stresses, respectively. Subsequently, the transition function is utilized to combine the two ANN models.

3.3.1 Construction of ANN model

The experimental true stress vs true plastic strain data at different temperatures and strain rates are extrapolated using the Voce (σ_V) and Ludwick (σ_L) laws, respectively. All extrapolated curves reach strain of 0.7.

$$\sigma_V = Y + Z \cdot [1 - \exp(-\gamma \cdot \varepsilon_p)] \tag{19}$$

$$\sigma_L = I + U \cdot \varepsilon_p^{\omega} \tag{20}$$

where Y, Z and γ are Voce parameters, and I, U and ω are Ludwick parameters. The values of the parameters are identified for each condition.

To prepare the data for ANN model training, the values of ε_p, T, $\ln(\dot{\varepsilon})$ and σ are normalized by

projecting them onto the interval [0.1, 0.9] [25]. The natural logarithmic form of the strain rate is adopted to ensure an even distribution of strain rate levels within the interval [45]. It linearizes the exponential relationship of strain rate effect making the network easier to learn and enhancing the stability of the training process. The normalization is performed using the following expression:

$$\begin{cases} x_i=[\varepsilon_{\mathrm{p}},\ T,\ \ln(\dot{\varepsilon}),\ \sigma] \\ x_i^{\mathrm{norm}}=0.1+0.8\cdot\dfrac{x_i-x_{i,\min}}{x_{i,\max}-x_{i,\min}} \end{cases} \tag{21}$$

where $x_{i,\min}$ and $x_{i,\max}$ represent the minimum and maximum values of the corresponding entries, respectively.

This work adopts a multi-layer feed-forward network implemented using the Tensorflow Python library. After testing various network architectures, an optimized architecture of 3-10-5-1 is adopted, which offers a good balance between complexity and accuracy for dataset and modeling needs. As illustrated in Fig. 19, the first layer is the input layer with three inputs, which are assigned the normalized ε_{p}, T and $\ln(\dot{\varepsilon})$. Followed by two hidden layers, the first hidden layer consisting of 10 neurons and the second one consisting of 5 neurons. The last layer with a single neuron is the output layer, which is used to output the predicted flow stress. Each neuron is equipped with its corresponding weight and bias, which control the signal propagation and transformation in the network. In detail, the transfers from the inputs to the first hidden layer are performed by multiplying each input with weight, and then adding the products to obtain a weighted sum and plus the bias of the corresponding neuron. The calculated value is then fed into an activation function to obtain the output of the neuron, which is passed to the next layer. The process is repeated until the final output is obtained. In this work, the sigmoid activation function is adopted, which introduces nonlinearity into the network to capture the complex relationships between inputs and output. In addition, the sigmoid function permits to calculate easily the derivatives of the output with respect to the three inputs. For the neuron in the output layer, no activation function is associated.

The constructed network architecture corresponds to a total of 101 parameters. The weights and biases of neurons are determined by training, which is a procedure of minimizing the cost-function. The cost-function quantifies the gap between the predicted output and the target output (normalized σ) using the mean square error (MSE). The Adam algorithm is employed to update the weights and biases during training. Both datasets (size: 25218) are split randomly into two subsets: a training set, and a test set, using a ratio of 8:2. The ANN model trained on the dataset generated by Voce law is referred to as Voce-ANN model, and the ANN trained on the dataset generated by Ludwick law is referred to as Ludwick-ANN model. After training, the cost-functions of both ANN models converge to a magnitude of 10^{-6}. To recover the physical meaning of the predicted output for the flow stress, an inverse normalization is performed using the following expression:

$$\sigma=\frac{\left(\sigma^{\mathrm{norm}}-0.1\right)\cdot\left(\sigma_{\max}-\sigma_{\min}\right)}{0.8}+\sigma_{\min} \tag{22}$$

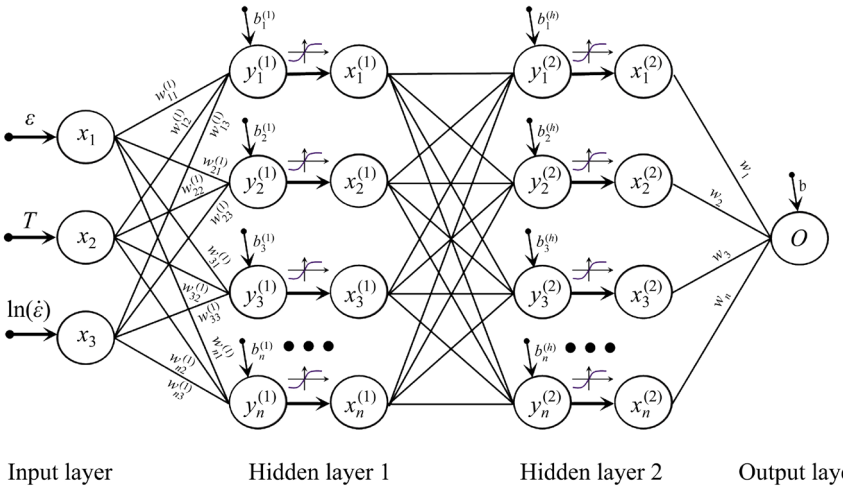

Fig. 19 Schematic diagram of multi-layer feed-forward network architecture

Figure 20 shows the predicted flow stress under different test conditions by the Voce-ANN model, and Fig. 21 shows the predictions by the Ludwick−ANN model. The predictions are in good agreement with the experimental flow stress. As expected, the predicted flow stress of the Voce-ANN model tends to saturate at large strain levels, and the one of the Ludwick−ANN model exhibits power law behavior. Both ANN models maintain the monotonic hardening of flow stress

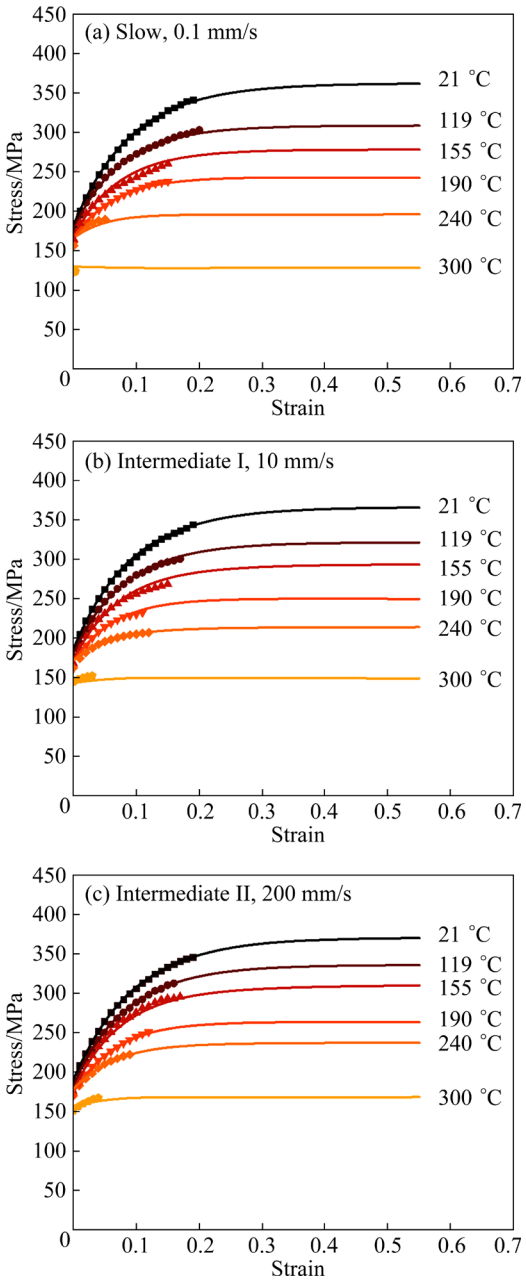

Fig. 20 Predicted flow stress curves (colored lines) by Voce-ANN model and experimental results (symbols) at different temperatures under slow (a), and intermediate I (b) and II (c) strain rate levels

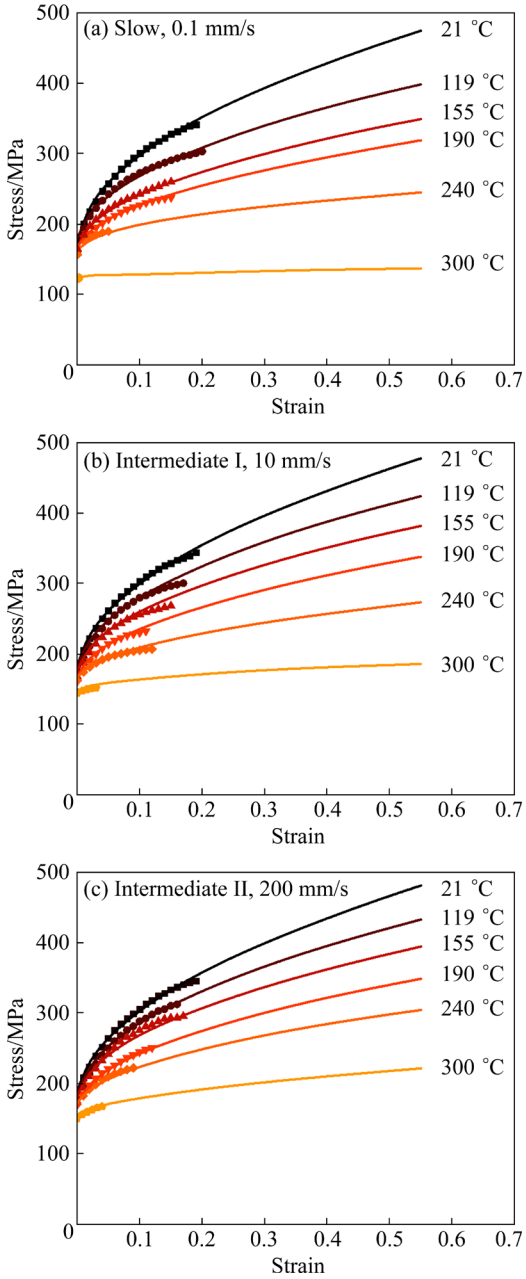

Fig. 21 Predicted flow stress curves (colored lines) by Ludwick-ANN model and experimental results (symbols) at different temperatures under slow (a), and intermediate I (b) and II (c) strain rate levels

with strain, except for a slight fluctuation observed in the Voce-ANN model under slow strain rate level at 300 °C. Despite the wide spacing of the three strain rates in the training dataset, the ANN model generates a smooth function to define the strain rate effect on flow stresses.

Figure 22(a) visualizes the identified strain rate effect through an example where the strain level is 0.3 and the temperature is 210 °C. It can be

seen that for strain rates beyond the range of the training set, the predictions of both ANN models remain reasonable (i.e., obeying to a logarithmic hardening form). The visualization of the identified temperature effect is shown in Fig. 22(b) for a given strain level of 0.3 and a strain rate of 10 s^{-1}. As expected from the experimental data, the two ANN models suggest highly nonlinear descriptions of the temperature effect within the range of the training set (from 21 to 300 °C), and the flow stresses decrease with the temperature increasing. However, for temperatures above 300 °C, the predictions of Voce-ANN model deviate from the actual behavior of the material. This means encountering a situation where the laws learned by the ANN model based on the training set fail to generalize out of the training range. Extending the range of data in the training set, optimizing the network structure according to the application [46], and adding physical constraints [47] to the training process are effective ways to improve the generalization capability of ANN. It should be noted that in this work, the network structure is determined with a focus on the prediction performance within the range of the training set. The ANN model is trained to minimize the cost-function for the flow stresses within the temperature range of the training set, and the good performance of the ANN model is evident within the range of the training set.

3.3.2 Calibration of transition function

The linear combination of the two ANN models is carried out by Eq. (23), where σ_{V-ANN} is defined by the Voce-ANN model and σ_{L-ANN} is defined by the Ludwick-ANN model. The linear combination coefficient (α) is defined using the transition function (Eq. (2)). The resulting combined model is referred to as the ML-based constitutive model. The ML-based model is implemented by a UMAT subroutine, and the associated flow-rule based on Yld2000-2D anisotropy yield criterion is employed. The flow stress derivatives are calculated analytically based on the chain-rule. The transition function is calibrated by hybrid experimental−numerical inverse analyses, same as the approach presented in Section 3.2.4. The calibrated parameters (P_i) are listed in Table 7, and the value of cost-function is optimized to 2.5%. The time-cost for the inverse identification procedure was about 70 h. The computation time with the ML-based model is about 3.2 min per FE job. The curve of the calibrated transition function is plotted in Fig. 23.

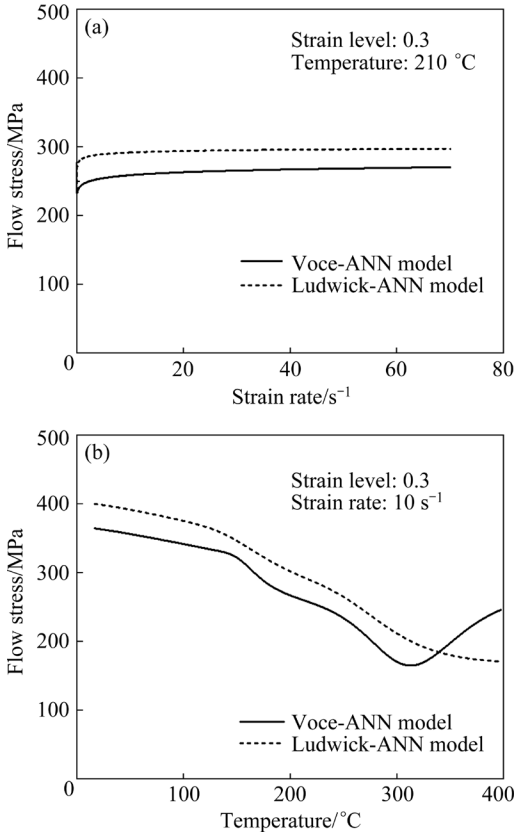

Fig. 22 (a) Visualization of identified strain rate effect at strain level of 0.3 and 210 °C; (b) Visualization of identified temperature effect at strain level of 0.3 and strain rate of 10 s^{-1}

Table 7 Calibrated parameters of transition function for ML-based constitutive model

P_1	P_2	P_3
0.61	1.27	23.31

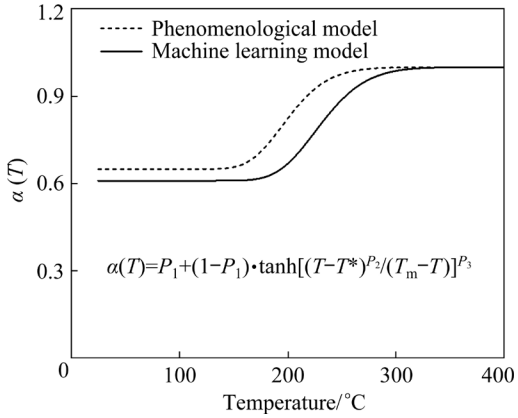

Fig. 23 Evolution of linear combination coefficient α with temperature for ML-based model (solid line) calculated with parameters listed in Table 7, and against with one for phenomenological model (dashed line)

The flow stresses under different test conditions predicted by the ML-based constitutive model are presented as colored lines in Fig. 24. The predicted hardening behavior shows an intermediate state between the power law and saturation below 155 °C, while it gradually transitions to saturation from 155 to 300 °C. This is similar to the findings from the phenomenological constitutive model. Figure 25 shows the predicted (colored lines) and experimental (symbols) F−D curves. For the slow strain rate level, a good agreement is obtained between the predictions and experiments. For the intermediate I and II strain rate levels, most predicted curves followed the experimental data well. For the 300 °C case, the plastic work leads to an increase in temperature at intermediate I and II strain rate levels, and the incorrect prediction of flow stresses by the Voce-ANN model at

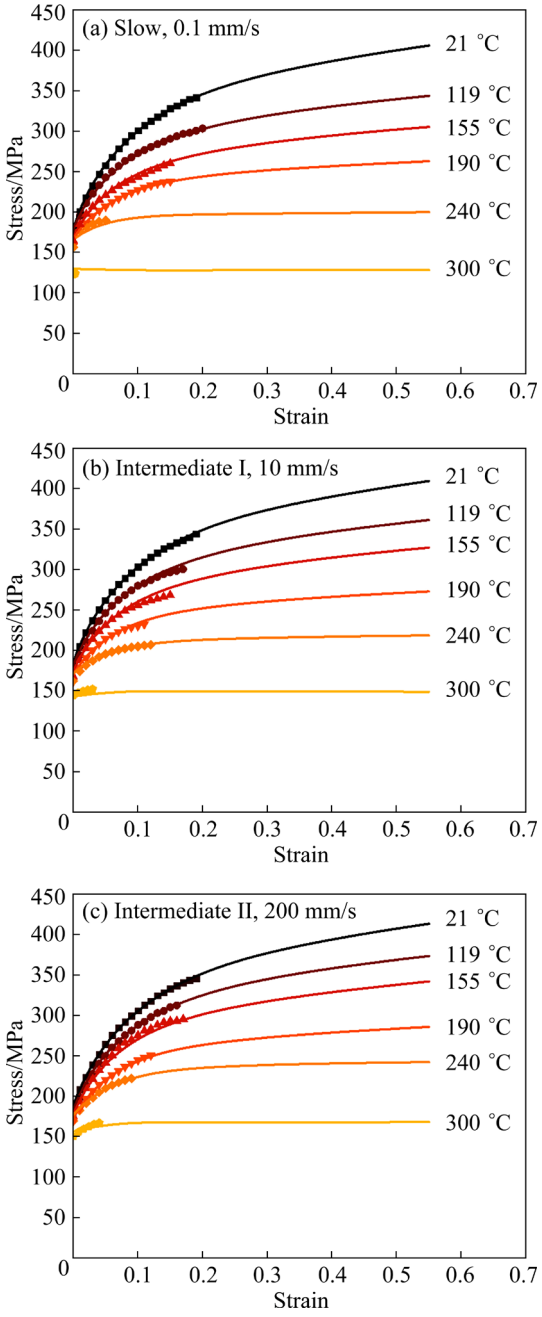

Fig. 24 Predicted flow stress curves (solid lines) by ML-based constitutive model and experimental results (symbols) at different temperatures under slow (a), and intermediate I (b) and II (c) strain rate levels

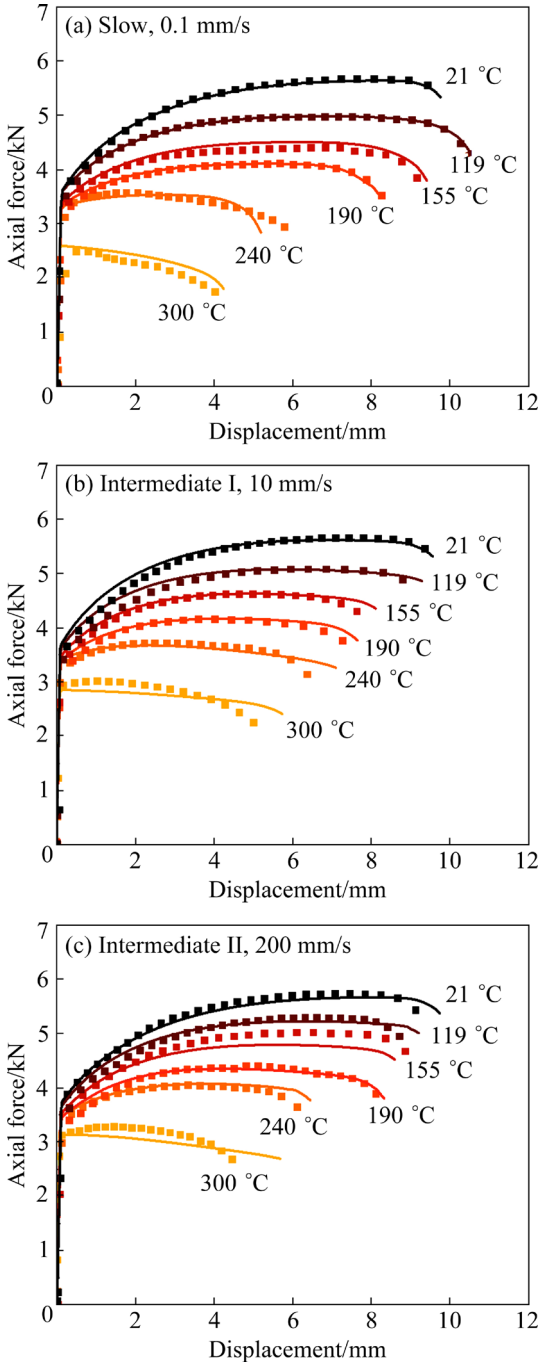

Fig. 25 Predicted (solid lines) and experimental (symbols) F−D curves for UT tests at slow (a), and intermediate I (b) and II (c) strain rate levels (The predictions are obtained by ML-based constitutive model)

temperatures above 300 °C leads to simulations that fail to reproduce necking.

$$\sigma=\alpha(T)\cdot\sigma_{\mathrm{V-ANN}}+[1-\alpha(T)]\cdot\sigma_{\mathrm{L-ANN}} \quad (23)$$

4 Conclusions

(1) The initial yield stress function allows to capture the non-monotonic evolution of initial yield stress with increasing temperature. By introducing a critical temperature associated with the micro-structural evolution of AA6061-T4 into constitutive equations, the highly nonlinear temperature and strain rate sensitivities are accurately represented. The transition of strain hardening behaviors from power-law to saturation types with increasing temperature is correctly predicted by inverse identification of the transition function. The phenomenological constitutive model provides reasonable predictions of the axial forces and necking in UT tests.

(2) The linear combination of two ANN models using the transition function provides an efficient solution for ML-based constitutive modelling. The ML-based model provides good representation of flow stresses within the training range, demonstrating the merits of ML in constitutive modeling. However, the predicted flow stresses deviate from the actual behavior of the material when the temperature exceeds the training range. This suggests that it is necessary to evaluate ML-based model in practical applications to ensure that its performance out of the training range also meets the requirements.

(3) Compared to the phenomenological model, the ML-based model gives a slightly lower value of the cost-function for the predictions of UT tests. ML provides a more convenient and efficient approach to constitutive modeling.

CRediT authorship contribution statement

Zhi-hao WANG: Conceptualization, Data curation, Methodology, Software, Investigation, Validation, Visualization, Writing − Original draft, Writing − Review & editing; **D. GUINES:** Supervision, Conceptualization, Data curation, Methodology, Software, Investigation, Validation, Writing − Review & editing; **Jia-shuo QI:** Data curation, Investigation, Writing − Review & editing; **Xing-rong CHU:** Investigation, Methodology, Writing − Review & editing; **L. LEOTOING:** Supervision, Project administration, Resource, Software, Conceptualization, Methodology, Investigation, Validation, Writing − Review & editing.

Declaration of competing interest

The authors declare that they have no known competing financial interests or personal relationships that could have appeared to influence the work reported in this paper.

Acknowledgments

Zhi-hao WANG acknowledges the China Scholarship Council (CSC) for his PhD financial support.

References

[1] TOROS S, OZTURK F, KACAR I. Review of warm forming of aluminum−magnesium alloys [J]. Journal of Materials Processing Technology, 2008, 207: 1−12.

[2] FAKIR O E, WANG L L, BALINT D, DEAR J P, LIN J G, DEAN T A. Numerical study of the solution heat treatment, forming, and in-die quenching (HFQ) process on AA5754 [J]. International Journal of Machine Tools and Manufacture, 2014, 87: 39−48.

[3] ZHOU Chang, ZHAN Li-hua, LI He, ZHAO Xing, CHEN Fei, HUANG Ming-hui. Creep ageing behaviour assisted by electropulsing under different stresses for Al−Cu−Li alloy [J]. Transactions of Nonferrous Metals Society of China, 2021, 31(7): 1916−1929.

[4] REZAEI ASHTIANI H R, SHAHSAVARI P. Constitutive modeling of flow behavior of precipitation-hardened AA7022-T6 aluminum alloy at elevated temperature [J]. Transactions of Nonferrous Metals Society of China, 2020, 30(11): 2927−2940.

[5] ZERILLI F J, ARMSTRONG R W. Dislocation-mechanics-based constitutive relations for material dynamics calculations [J]. Journal of Applied Physics, 1987, 61: 1816−1825.

[6] VOYIADJIS G Z, ABED F H. Microstructural based models for bcc and fcc metals with temperature and strain rate dependency [J]. Mechanics of Materials, 2005, 37: 355−378.

[7] LIU X, XU P, ZHAO J, LU W, LI M, WANG G. Material machine learning for alloys: Applications, challenges and perspectives [J]. Journal of Alloys and Compounds, 2022, 921: 165984.

[8] WANG Y, XING J, ZHOU Y, KONG C, YU H. Tensile properties and a modified s-Johnson−Cook model for constitutive relationship of AA7075 sheets at cryogenic temperatures [J]. Journal of Alloys and Compounds, 2023, 942: 169044.

[9] HUH H, AHN K, LIM J H, KIM H W, PARK L J. Evaluation of dynamic hardening models for BCC, FCC, and HCP metals at a wide range of strain rates [J]. Journal of Materials Processing Technology, 2014, 214: 1326−1340.

[10] PIAO M J, HUH H, LEE I, PARK L. Characterization of hardening behaviors of 4130 Steel, OFHC Copper, Ti6Al4V alloy considering ultra-high strain rates and high temperatures [J]. International Journal of Mechanical Sciences, 2017,

131/132 : 1117−1129.

[11] KHAN A S, BAIG M. Anisotropic responses, constitutive modeling and the effects of strain-rate and temperature on the formability of an aluminum alloy [J]. International Journal of Plasticity, 2011, 27: 522−538.

[12] KHAN A S, LIU H W. Variable strain rate sensitivity in an aluminum alloy: Response and constitutive modeling [J]. International Journal of Plasticity, 2012, 36: 1−14.

[13] SUNG J H, KIM J H, WAGONER R H. A plastic constitutive equation incorporating strain, strain-rate, and temperature [J]. International Journal of Plasticity, 2010, 26: 1746−1771.

[14] MARTINS J M P, THUILLIER S, ANDRADE-CAMPOS A. Calibration of a modified Johnson−Cook model using the Virtual Fields Method and a heterogeneous thermo-mechanical tensile test [J]. International Journal of Mechanical Sciences, 2021, 202/203: 106511.

[15] XIAO X K, MU Z C, PAN H, LOU Y S. Effect of the Lode parameter in predicting shear cracking of 2024-T351 aluminum alloy Taylor rods [J]. International Journal of Impact Engineering, 2018, 120: 185−201.

[16] ENGLER O. Effect of precipitation state on plastic anisotropy in sheets of the age-hardenable aluminium alloys AA 6016 and AA 7021 [J]. Materials Science and Engineering: A, 2022, 830: 142324.

[17] MYHR O R, GRONG Ø, ANDERSEN S J. Modelling of the age hardening behaviour of Al−Mg−Si alloys [J]. Acta Materialia, 2001, 49: 65−75.

[18] GHOSH M, MIROUX A, KESTENS L A I. Experimental study and modelling of the role of solutes, precipitates and temperature on the work-hardening of AA6xxx aluminium alloys [J]. Materials Science and Engineering: A, 2021, 805: 140615.

[19] KREYCA J, KOZESCHNIK E. Temperature-dependent strain hardening, precipitation and deformation-induced microstructure evolution in AA 6061 [J]. Materials Science and Engineering : A, 2017, 708: 411−418.

[20] AVRIL S, BONNET M, BRETELLE A S, GRÉDIAC M, HILD F, IENNY P, LATOURTE F, LEMOSSE D, PAGANO S, PAGNACCO E, PIERRON F. Overview of identification methods of mechanical parameters based on full-field measurements [J]. Experimental Mechanics, 2008, 48: 381−402.

[21] LANG Li-hui, LI Tao, ZHOU Xian-bin, KRISTENSEN B E, DANCKERT J, NIELSEN K B. Optimized constitutive equation of material property based on inverse modeling for aluminum alloy hydroforming simulation [J]. Transactions of Nonferrous Metals Society of China, 2006, 16(6): 1379−1385.

[22] SCHLEDER G R, PADILHA A C M, ACOSTA C M, COSTA M, FAZZIO A. From DFT to machine learning: recent approaches to materials science—A review [J]. Journal of Physics: Materials, 2019, 2: 032001.

[23] ZAMANI M R, MIRZADEH H, MALEKAN M. Artificial neural network applicability in studying hot deformation behaviour of high-entropy alloys [J]. Materials Science and Technology, 2023, 39(18): 3351−3359.

[24] WANG D X, ZHU Q Q, WEI Z X, LIN B S, JING Y, SHI Y, MISRA R D K, LI J P. Hot deformation behaviors of AZ91 magnesium alloy: Constitutive equation, ANN-based prediction, processing map and microstructure evolution [J]. Journal of Alloys and Compounds, 2022, 908: 164580.

[25] SANTOSH S, SAMPATH V, MOULISWAR R R. Hot deformation characteristics of NiTiV shape memory alloy and modeling using constitutive equations and artificial neural networks [J]. Journal of Alloys and Compounds, 2022, 901: 163451.

[26] LIU X J, ZHANG H Y, ZHANG S, PENG W, ZHOU G, WANG C, CHEN L J. Hot deformation behavior of near-β titanium alloy Ti−3Mo−6Cr−3Al−3Sn based on phenomenological constitutive model and machine learning algorithm [J]. Journal of Alloys and Compounds, 2023, 968: 172052.

[27] LI X Y, ROTH C C, BONATTI C, MOHR D. Counterexample- trained neural network model of rate and temperature dependent hardening with dynamic strain aging [J]. International Journal of Plasticity, 2022, 151: 103218.

[28] XU J B, HOLMEDAL B, HOPPERSTAD O S, MÁNIK T, MARTHINSEN K. Dynamic strain ageing in an AlMg alloy at different strain rates and temperatures: Experiments and constitutive modelling [J]. International Journal of Plasticity, 2022, 151: 103215.

[29] SAADA G. Cross-slip and work hardening of f.c.c. crystals [J]. Materials Science and Engineering: A, 1991, 137: 177−183.

[30] LI Y L, KOHAR C P, MUHAMMAD W, INAL K. Precipitation kinetics and crystal plasticity modeling of artificially aged AA6061 [J]. International Journal of Plasticity, 2022, 152: 103241.

[31] MURAYAMA M, HONO K. Pre-precipitate clusters and precipitation processes in Al−Mg−Si alloys [J]. Acta Materialia, 1999, 47: 1537−1548.

[32] NINIVE P H, STRANDLIE A, GULBRANDSEN-DAHL S, LEFEBVRE W, MARIOARA C D, ANDERSEN S J, FRIIS J, HOLMESTAD R, LØVVIK O M. Detailed atomistic insight into the β'' phase in Al−Mg−Si alloys [J]. Acta Materialia, 2014, 69: 126−134.

[33] CHEN J H, COSTAN E, VAN HUIS M A, XU Q, ZANDBERGEN H W. Atomic pillar-based nanoprecipitates strengthen AlMgSi alloys [J]. Science, 2006, 312: 416−419.

[34] KREYCA J, KOZESCHNIK E. State parameter-based constitutive modelling of stress strain curves in Al−Mg solid solutions [J]. International Journal of Plasticity, 2018, 103: 67−80.

[35] RUSINEK A, KLEPACZKO J R. Shear testing of a sheet steel at wide range of strain rates and a constitutive relation with strain-rate and temperature dependence of the flow stress [J]. International Journal of Plasticity, 2001, 17: 87−115.

[36] SHEN F H, MÜNSTERMANN S, LIAN J H. An evolving plasticity model considering anisotropy, thermal softening and dynamic strain aging [J]. International Journal of Plasticity, 2020, 132: 102747.

[37] LIN M R, WAGONER R H. An experimental investigation of deformation induced heating during tensile testing [J]. Metallurgical and Materials Transactions A, 1987, 18: 1035−1042.

[38] MOLINARI A, RAVICHANDRAN G. Constitutive modeling of high-strain-rate deformation in metals based on the evolution of an effective microstructural length [J].

Mechanics of Materials, 2005, 37: 737−752.
[39] KHAN A S, SUH Y S, KAZMI R. Quasi-static and dynamic loading responses and constitutive modeling of titanium alloys [J]. International Journal of Plasticity, 2004, 20: 2233−2248.
[40] ZHANG C, LOU Y S, ZHANG S J, CLAUSMEYER T, TEKKAYA A E, FU L, CHEN Q, ZHANG Q. Large strain flow curve identification for sheet metals under complex stress states [J]. Mechanics of Materials, 2021, 161: 103997.
[41] JOUN M, CHOI I, EOM J, LEE M. Finite element analysis of tensile testing with emphasis on necking [J]. Computational Materials Science, 2007, 41: 63−69.
[42] ROY B K, KORKOLIS Y P, ARAI Y, ARAKI W, IIJIMA T, KOUYAMA J. Plastic deformation of AA6061-T6 at elevated temperatures: Experiments and modeling [J]. International Journal of Mechanical Sciences, 2022, 216: 106943.
[43] GAO J X, GAO Y Z, LU L H, HU Z J, WANG K J, GUO F, YAN Y D. Study on the interaction between nanosecond laser and 6061 aluminum alloy considering temperature dependence [J]. Journal of Alloys and Compounds, 2022, 892: 162044.
[44] BARLAT F, BREM J C, YOON J W, CHUNG K, DICK R E, LEGE D J, POURBOGHRAT F, CHOI S H, CHU E. Plane stress yield function for aluminum alloy sheets—Part 1: Theory [J]. International Journal of Plasticity, 2003, 19: 1297−1319.
[45] PANTALÉ O, MHA P T, TONGNE A. Efficient implementation of non-linear flow law using neural network into the Abaqus Explicit FEM code [J]. Finite Elements in Analysis and Design, 2022, 198: 103647.
[46] LINKA K, KUHL E. A new family of Constitutive Artificial Neural Networks towards automated model discovery [J]. Computer Methods in Applied Mechanics and Engineering, 2023, 403: 115731.
[47] MASI F, STEFANOU I, VANNUCCI P, MAFFI-BERTHIER V. Thermodynamics-based artificial neural networks for constitutive modeling [J]. Journal of the Mechanics and Physics of Solids, 2021, 147: 104277.

基于现象学和机器学习方法预测 AA6061-T4 板材与温度和应变速率相关的流动行为

王志豪[1]，D. GUINES[1]，戚嘉硕[2]，褚兴荣[3]，L. LEOTOING[1]

1. Univ Rennes, INSA Rennes, LGCGM (Laboratoire de Génie Civil et Génie Mécanique) - EA 3913, F-35000 Rennes, France;
2. Alliance Sorbonne Université, Université de Technologie de Compiègne,
Laboratoire Roberval, CS 60319, Compiègne Cedex, France;
3. 山东大学 机电与信息工程学院，威海 264209

摘　要：研究 AA6061-T4 板材在不同温度(21～300 ℃)和应变速率(0.002～4 s^{-1})下的塑性流动行为。揭示温度和应变速率对流动应力的显著非线性影响，以及潜在的微观机制。开发了基于现象学和机器学习的本构模型。两种模型建立在由过渡函数调节的线性组合框架内，可捕捉应变硬化行为随温度升高而发生的演变。为现象学本构模型制定了用于描述温度和应变速率敏感性的新数学函数，并考虑了与显微组织演变相关的阈值温度。采用通过经典应变硬化律外推实验数据的数据丰富策略来优化神经网络训练。提出了一种仅关注过渡函数的高效逆向识别策略，以提高本构模型对材料缩颈后变形行为的预测精度。

关键词：AA6061-T4 板材；热黏塑性；本构模型；机器学习；应变速率和温度效应

(Edited by Xiang-qun LI)